Potentially multiferroic Aurivillius phase $Bi_5FeTi_3O_{15}$: Cation site preference, electric polarization, and magnetic coupling from first principles

Axiel Yaël Birenbaum* and Claude Ederer†
Materials Theory, ETH Zürich, Wolfgang-Pauli-Strasse 27, 8093 Zürich, Switzerland
(Received 17 July 2014; revised manuscript received 3 October 2014; published 22 December 2014)

We study the structural, ferroelectric, and magnetic properties of the potentially multiferroic Aurivillius phase material $Bi_5FeTi_3O_{15}$ using first-principles electronic structure calculations. Calculations are performed both with PBE and PBEsol exchange correlation functionals. We conclude that PBE systematically overestimates the lattice constants and the magnitude of the ferroelectric distortion, whereas PBEsol leads to good agreement with available experimental data. We then assess a potential site preference by comparing ten different distributions of the Fe^{3+} cation on the perovskite B sites. We find a slight preference for the "inner" site, consistent with recent experimental observations. We obtain a large value of $\sim 55\ \mu C/cm^2$ for the spontaneous electric polarization, which is rather independent of the specific Fe distribution. Finally, we calculate the strength of the magnetic coupling constants and find strong antiferromagnetic coupling between Fe^{3+} cations in nearest-neighbor positions, whereas the coupling between further neighbors is rather weak. This poses the question whether magnetic long-range order can occur in this system in spite of the low concentration of magnetic ions.

DOI: 10.1103/PhysRevB.90.214109 PACS number(s): 75.85.+t, 77.80.−e, 75.47.Lx, 75.30.Et

I. INTRODUCTION

Multiferroic materials, which exhibit simultaneous ferroelectric and magnetic order, have been attracting considerable attention during the last decade [1–5]. Much of the corresponding research is motivated by the great potential of these materials for non-volatile data storage, sensor applications, and many other areas of technology. However, materials that exhibit multiferroic properties above room temperature, and are thus suitable candidates for future device applications, are still extremely scarce. The search for alternative materials with robust multiferroic properties above room temperature is therefore of high relevance.

One possible route for the design of novel multiferroic materials is to start from a series of well-established ferroelectrics and create additional functionality by incorporating magnetic ions into these systems. A promising class of materials for this purpose are the so-called *Aurivillius phases*. The Aurivillius phases are a family of compounds that form in a naturally layered perovskite-related crystal structure which consists of m perovskite layers $(A_{m-1}B_mO_{3m+1})^{2-}$, stacked along the [001] direction, and separated by fluoritelike $(Bi_2O_2)^{2+}$ layers (see Fig. 1 for an example with $m = 4$). The overall chemical composition is thus $Bi_2A_{m-1}B_mO_{3m+3}$, where many different cations can be incorporated on the A and B sites within the perovskitelike layers [7]. The Aurivillius phases are well known for their excellent ferroelectric properties with very low fatigue [8,9], and offer great potential for tailoring specific properties by varying both ionic composition and number of layers.

A number of Aurivillius compounds exhibiting multiferroic properties have been reported recently. For example, room temperature ferromagnetism together with ferroelectric polarization has been reported for materials based on the four-layer compound $Bi_5FeTi_3O_{15}$, but with half of the Fe cations substituted by either Co or Ni [10,11]. Furthermore, magnetic field-induced ferroelectric domain switching has recently been observed in a five-layer system with composition $Bi_6Ti_{2.8}Fe_{1.52}Mn_{0.68}O_{18}$ [12]. However, it should be noted that in many cases the observed polarization and magnetization depend strongly on the synthesis method and annealing conditions [13,14], and it has been pointed out that the weak magnetic signals found in these samples can indeed be caused by tiny inclusions of other phases, which are extremely hard to detect using standard characterization methods [15].

Even in the case of $Bi_5FeTi_3O_{15}$, the "parent compound" for many of the compositions that have been explored as potential multiferroics, the ferroelectric and magnetic properties are not well established. An antiferromagnetic Néel temperature of 80 K has been reported [16]. However, several more recent studies show paramagnetic behavior with no magnetic long-range order even at very low temperatures [13,17–19]. Fits of magnetic susceptibility data have found conflicting signs of the Curie-Weiss temperature in different samples, indicating either ferromagnetic [13] or antiferromagnetic [17,19] interactions between the Fe cations. Similarly, no well-established value exists for the spontaneous electric polarization in $Bi_5FeTi_3O_{15}$, due to difficulties in obtaining fully saturated ferroelectric hysteresis loops. Reported values for the remanent polarization vary from 3.5 to $\sim 30\ \mu C/cm^2$ [13,14].

It is therefore desirable to establish the intrinsic properties of $Bi_5FeTi_3O_{15}$ and other potentially multiferroic Aurivillius phases using modern first-principles electronic structure calculations. Such calculations provide a useful reference for experimental observations and can also be used as guideline for future studies.

Here we present results of such first-principles calculations for the four-layer Aurivillius phase $Bi_5FeTi_3O_{15}$. We show that the structural properties of this material can be obtained in good agreement with available experimental data using the PBEsol functional for the exchange-correlation energy. We also show that there is a preference for the Fe^{3+} cation to occupy the "inner" sites within the perovskitelike layers, and we suggest the possibility to reverse this preference using

*yael.birenbaum@mat.ethz.ch
†claude.ederer@mat.ethz.ch

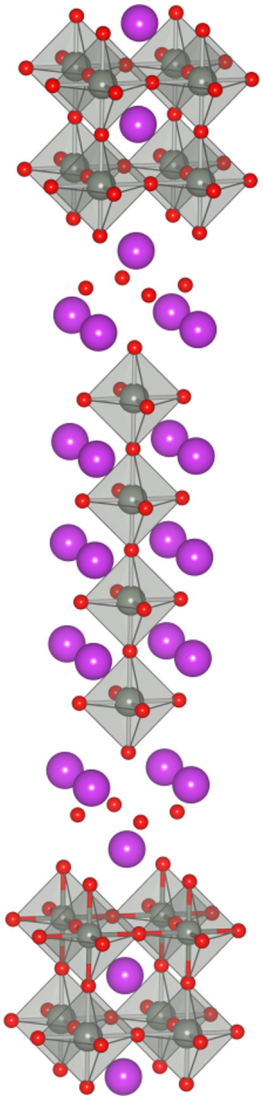

FIG. 1. (Color online) High-symmetry tetragonal crystal structure of $Bi_5FeTi_3O_{15}$ (space group $I4/mmm$), corresponding to $m = 4$ in the Aurivillius series. Four perovskitelike layers are stacked along [001] and separated by fluoritelike $(Bi_2O_2)^{2-}$ layers. Bi and O atoms are shown as large and small (purple and red) spheres, respectively, whereas the Fe/Ti atoms are located inside the gray octahedra. Note that each perovskite block is offset relative to the next one by $(\frac{a_0}{2}, \frac{a_0}{2}, \frac{c_0}{2})$, where a_0 and c_0 are the lattice parameters of the conventional tetragonal unit cell. This picture has been generated using VESTA [6].

epitaxial strain. Furthermore, we calculate a large spontaneous ferroelectric polarization of $\sim$55 $\mu C/cm^2$, which is similar in magnitude to the related three-layer system $Bi_4Ti_3O_{12}$. This shows that the presence of the magnetic Fe^{3+} cations is not detrimental to the ferroelectric properties of $Bi_5FeTi_3O_{15}$. Finally, we calculate the strength of the magnetic coupling and find a very strong and antiferromagnetic coupling between Fe in nearest-neighbor positions. However, the coupling becomes nearly negligible beyond second neighbors, consistent with the short range character of the underlying superexchange mechanism. This leaves the question of whether long-range magnetic order can be expected in $Bi_5FeTi_3O_{15}$ open for future studies.

This paper is organized as follows. In the next section, we present the method we use in our first-principles calculations, and discuss in particular how we treat the quasi-random distribution of Fe^{3+} and Ti^{4+} cations over the available sites within the perovskitelike layers. In Secs. III A and III B, we then present our results for the structural properties and the energetics of the different cation distributions. Section III C focuses on the calculation of the electric polarization, and in Sec. III D, we give a brief discussion of the electronic structure in $Bi_5FeTi_3O_{15}$. Finally, in Sec. III E, we present our analysis of the calculated magnetic coupling constants and discuss the possibility of long-range magnetic order. A summary and some further conclusions are given in Sec. IV.

II. METHODS

A. Aurivillius crystal structure and different distributions of Fe/Ti cations

Most members of the homologous series of Aurivillius compounds exhibit a tetragonal structure with space group symmetry $I4/mmm$ at high temperatures (see Fig. 1 for the case of $m = 4$). On cooling, this structure transforms into a polar structure corresponding to a subgroup symmetry of $I4/mmm$. Even-layered Aurivillius phases such as $Bi_5FeTi_3O_{15}$ (i.e., $m = 2,4,\ldots$) transform to orthorhombic symmetry $A2_1am$ (space group No. 36), whereas odd-layered members ($m = 1,3,\ldots$) transform into $B2cb$ symmetry (space group No. 41) or an even lower symmetry corresponding to a subgroup of $B2cb$ [7,20]. The symmetry lowering from $I4/mmm$ to $A2_1am$ leads to a doubling of the primitive unit cell, with two formula units (48 atoms) per unit cell in the $A2_1am$ structure.

There are two inequivalent B sites in the four-layer structure: the *inner* sites within the perovskite layers, and the *outer* sites adjacent to the Bi_2O_2 layers. In $Bi_5FeTi_3O_{15}$, these octahedrally coordinated B sites are shared between the Fe^{3+} and Ti^{4+} cations, and a quasi-random cation distribution is observed in experiments [21]. However, recent Mössbauer experiments have reported a slight preference of Fe^{3+} to occupy the inner sites within the perovskite layers, whereas the outer sites are preferentially occupied by Ti^{4+} cations [22].

In our calculations for $Bi_5FeTi_3O_{15}$ we use the 48 atom unit cell corresponding to the primitive unit cell of the low-symmetry $A2_1am$ structure, which contains eight octahedrally-coordinated B sites (four inner and four outer sites). There are ten symmetrically inequivalent ways to distribute two Fe and six Ti atoms over these eight B sites, all of which are depicted in Table I. In this work, we explicitly consider each of the ten individual configurations listed in Table I. This allows us to evaluate the impact of a specific cation distribution on the physical properties and also to address a potential site preference of the Fe^{3+} and Ti^{4+} cations in $Bi_5FeTi_3O_{15}$. We note that the specific distribution of cations breaks further symmetries compared to the experimental $A2_1am$ structure. One could think of the latter as a weighted average over all the possible configurations.

To allow for all distortions observed in the experimental $A2_1am$ symmetry, we use lattice vectors that resemble the corresponding base-centered orthorhombic lattice vectors.

TABLE I. (Color online) The ten symmetrically inequivalent configurations considered in this work, corresponding to different distributions of Fe and Ti over the octahedral B sites. Fe and Ti sites are indicated by dark (brown) and light (blue) octahedra, respectively. The configurations are grouped into "outer," "mixed," and "inner," depending on whether two, one, or none of the two Fe cations in the unit cell are situated in the perovskite layers adjacent to the Bi_2O_2 layers. The notation defined in the second line is used throughout this paper to denote the various configurations.

"outer"			"mixed"				"inner"		
O1	O2	O3	M1	M2	M3	M4	I1	I2	I3
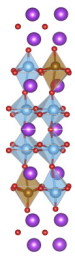	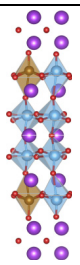	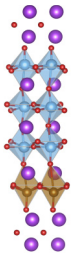	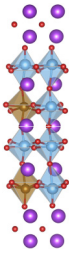	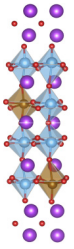	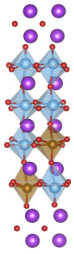	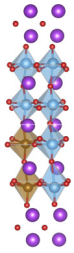	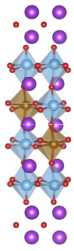	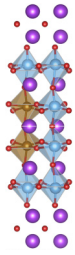	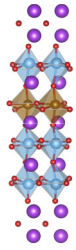

In other words, $\vec{a} \approx (\sqrt{2}a_0,0,0)$, $\vec{b} \approx (0,\sqrt{2}a_0,0)$, and $\vec{c} \approx (\sqrt{2}a_0/2,0,c_0/2)$, where a_0 and c_0 correspond to the in-plane and out-of-plane lattice constants of the high-symmetry $I4/mmm$ structure.[1] Due to the lower symmetry of the individual cation configurations listed in Table I, we obtain small deviations from the ideal base-centered orthorhombic lattice after relaxation. Specifically, the angles between the lattice vectors deviate slightly from the angles within perfect orthorhombic symmetry. However, in all cases, these deviations are smaller than 0.7°.

B. Computational details

We perform first-principles calculations using density functional theory (DFT) and the projector augmented wave (PAW) method as implemented in the Vienna *ab initio* simulation package (VASP) [23,24]. We use the generalized gradient approximation according to Perdew, Burke, and Ernzerhof (PBE) and its version optimized for solids (PBEsol) [25,26]. We use PAW potentials that include 15 valence electrons for Bi ($6s^2 5d^{10} 6p^3$), 14 for Fe ($3p^6 4s^2 3d^6$), 10 for Ti ($3p^6 4s^2 3d^2$), and 6 for O ($2s^2 2p^4$). To correctly treat the strong interactions between the Fe-d electrons, the Hubbard "$+U$" correction was applied with $U_{\mathrm{Fe}} = 3.0$ eV and the Hund's coupling parameter J_H set to zero [27]. This value for U_{Fe} lies in the typical range that has been used successfully to describe various properties of $BiFeO_3$ [28–31]. Some calculations with $U_{\mathrm{Fe}} = 5$ eV are also performed to assess the sensitivity of electronic structure and magnetic coupling constants on the magnitude of U_{Fe}.

We perform full structural relaxations of all degrees of freedom (lattice parameters and internal positions) for all ten configurations listed in Table I, both with parallel and antiparallel orientation of the magnetic moments of the two Fe^{3+} cations within the unit cell. Lattice parameters and ionic positions are relaxed until the residual forces are smaller than 10^{-3} eV/Å and the total energy changes less than 10^{-8} eV. Calculations are converged using a Γ-centered k-point mesh with $4 \times 4 \times 2$ divisions along the three reciprocal lattice vectors and a plane wave cutoff energy of $E_{\mathrm{cut}} = 550$ eV. For the calculation of the electronic density of states, a denser (and more uniform) $12 \times 12 \times 3$ k-point mesh is used.

[1]Note that strictly speaking the space group notation $A2_1am$ implies a setting where the polar screw axis 2_1 is along the $\vec{a}$ direction, whereas in our calculations we use a setting with the polar axis along $\vec{b}$. For consistency with the literature, we nevertheless use $A2_1am$ to denote space group No. 36 within this paper.

III. RESULTS AND DISCUSSION

A. Lattice parameters and energetics

In this section, we present the energies and lattice parameters obtained by full structural relaxation of all ten symmetrically inequivalent configurations with different distributions of Fe^{3+} and Ti^{4+} cations listed in Table I. All presented results are obtained for antiparallel alignment of the Fe magnetic moments. As will be shown in Sec. III E this corresponds to the preferred magnetic state in all cases.

Figure 2 shows the lengths of the three lattice vectors obtained after full structural relaxation for each configuration, in comparison with experimental data taken from Ref. [21]. One can see that for both PBE and PBEsol there is a clear correlation between the lattice constants and the distribution of Fe^{3+} and Ti^{4+} cations over the available B sites. The three inner configurations have longer in-plane lattice constants, a and b, and shorter out-of-plane constants, c, compared to the three outer configurations. Mixed configurations are in between these two cases. Differences between configurations of the same "type" (i.e., inner, outer, or mixed) are rather small.

The larger tetragonality (larger c/a) of the crystallographic unit cell for the outer configurations is related to a consistently large *local* tetragonality of the Fe sites in the outer perovskite layer. For the following, we define the local tetragonality of the perovskite sites as the ratio between the out-of-plane and in-plane O-O distances, $d_\perp/d_\parallel$, of the surrounding oxygen octahedron. For the outer Fe sites, averaged over the three outer configurations (O1-O3), we obtain $d_\perp/d_\parallel = 1.21$ within PBE and $d_\perp/d_\parallel = 1.16$ within PBEsol. In contrast, the average outer site tetragonality with all Fe occupying the inner site (I1-I3) is only $d_\perp/d_\parallel = 1.04$ with either exchange correlation functional. Furthermore, in all outer and mixed configurations the local tetragonality of the outer Fe sites is consistently

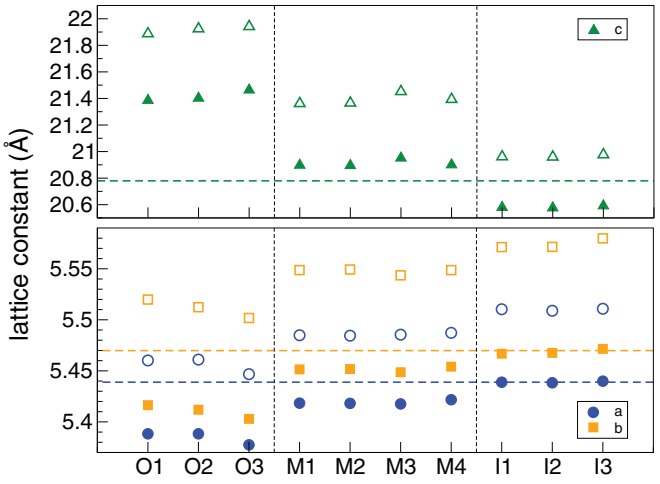

FIG. 2. (Color online) Lengths of the three lattice vectors $a = |\vec{a}|$ (bottom, circles), $b = |\vec{b}|$ (bottom, squares), and $c = |\vec{c}|$ (top, triangles) for the ten different configurations listed in Table I, computed using the PBEsol (filled symbols) and the PBE (open symbols) functionals. The horizontal dashed lines correspond to experimental data from Ref. [21].

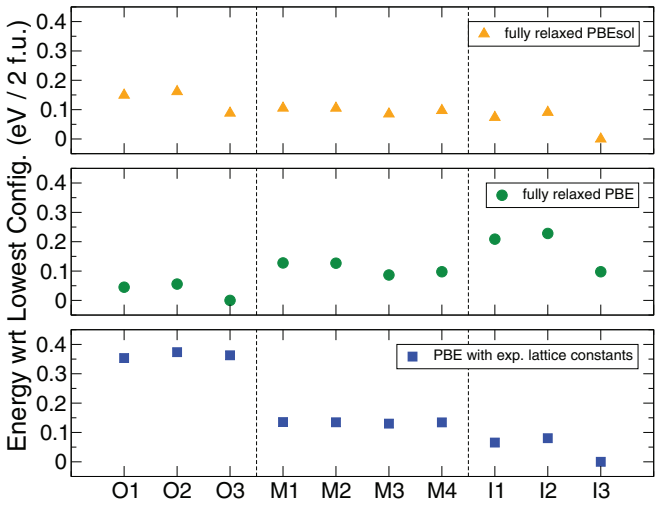

FIG. 3. (Color online) Relative energies of all configurations for the three cases discussed in the main text: full relaxation using PBEsol (top), full relaxation using PBE (middle), and only ionic positions relaxed using PBE with lattice parameters fixed to experimental values (bottom).

larger than that of the outer Ti sites. The local tetragonality of the inner perovskite sites is always close to 1 (average $d_\perp/d_\parallel = 1.01$ within PBEsol).

It is interesting to note that the large tetragonal distortion of the oxygen octahedron together with the large off-center displacement of the Fe^{3+} cation on the outer site leads to a quasi-fivefold square-pyramid coordination of Fe^{3+} that closely resembles the "super-tetragonal" phase found in thin films of $BiFeO_3$ under strong compressive strain [30,32,33].

While both PBE and PBEsol exhibit the same qualitative trends, the level of agreement with the experimental lattice parameters is different for the two functionals. Generally, PBEsol leads to slightly smaller lattice parameters compared to PBE, and overall seems to provide better agreement with the experimental data. The best agreement is observed for the inner and mixed configurations using PBEsol. On average (over all configurations), PBE overestimates a, b, and c by 0.05 (0.8%), 0.08 (1.4%), and 0.63 Å (3.1%), respectively, whereas PBEsol underestimates both a and b by 0.02 Å (0.4%), and overestimates c by 0.18 Å (0.8%).

We also verified that the specific value of the Hubbard U does not have a noticeable effect on the structural properties. Within PBEsol, an increase of the Hubbard U applied on the Fe site from $U_{Fe} = 3$ to 5 eV leads to differences in lattice constants and volume of not more than 0.07%.

In order to identify a possible site preference of the Fe^{3+} cation, we next compare the relative energies per unit cell for all configurations. To estimate the effect of the slight under- or overestimation of the lattice parameters compared to the experimental values, we consider three distinct cases: (i) full structural relaxation using the PBEsol functional, (ii) full relaxation using PBE, and (iii) lattice parameters fixed to the experimental values from Ref. [21] and internal atomic coordinates relaxed using PBE. We find that in all three cases, the energies of the different configurations form a hierarchy according to the classification of the Fe distribution as inner, outer, and mixed (see Fig. 3). This indicates that the main factor determining the energetics is the total amount of Fe sitting in the inner (or outer) perovskite layers and that the specific spatial distribution within each layer is less important. It can further be seen that the full PBEsol relaxations, which give the best agreement with the experimental lattice constants, indicate a preference of the Fe^{3+} cations to occupy the inner site, whereas the full PBE relaxations, which slightly overestimate the lattice constants, prefer Fe on the outer sites. Interestingly, the calculations where the lattice parameters have been fixed to experimental values and only the internal positions of the ions are relaxed using PBE gives the same site preference as PBEsol, i.e., lower energies for the inner configurations. Therefore the slight overestimation of the lattice parameters within PBE seems to be responsible for the different site preference obtained within PBE and PBEsol. This sensitivity of the observed site preference on the lattice parameters as well as the more elongated unit cell (larger c/a ratio) obtained for the outer configurations (see Fig. 2) suggest a potential way of tailoring the cation distribution using epitaxial strain, i.e., by growing thin films of $Bi_5FeTi_3O_{15}$ on different substrates with either positive or negative lattice mismatch.

As can be seen from Fig. 3, the energy differences between different cation configurations are of the order of ∼100 meV per unit cell. To obtain a rough estimate of whether these energy differences can lead to noticeable deviations from a random distribution of Fe^{3+} and Ti^{4+} cations over the octahedral sites, we calculate the Fe occupation of the outer site as a thermal average,

$$\langle c_{Fe}^{(out)} \rangle (T) = \frac{1}{Z} \sum_i c_{Fe,i}^{(out)} e^{-E_i/k_B T}, \qquad (1)$$

where E_i and $c_{Fe,i}^{(out)}$ are the energy and outer site occupation of configuration i, and $Z = \sum_i e^{-E_i/k_B T}$.

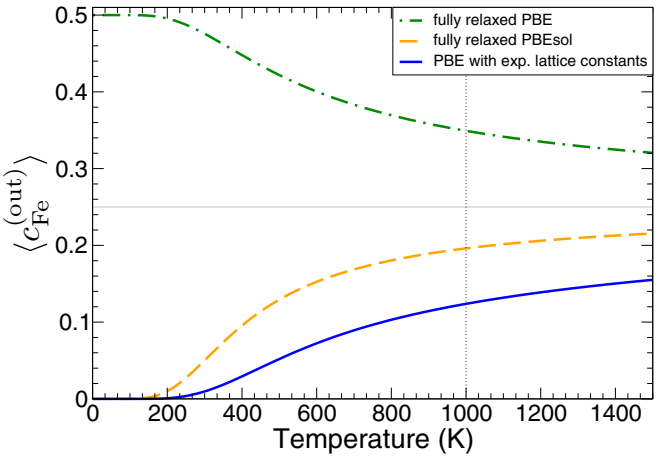

FIG. 4. (Color online) Thermal average of the Fe occupation on the outer site for the three different cases discussed in the text. The vertical dotted line indicates a typical growth temperature of 1000 K. The horizontal dashed line indicates the value of 0.25 corresponding to a completely random cation distribution.

We note that this is a simplified model that considers only the 10 configurations that correspond to our choice of periodic unit cell and does not take into account any kinetic effects during growth. We therefore do not expect it to accurately predict the outer site occupation in realistic samples. Nevertheless, this model gives a rough idea of the temperature range in which a preferential site occupation can be expected based on simple energetics.

Figure 4 shows the resulting temperature dependence of $\langle c_{Fe}^{(out)} \rangle$, i.e., the average Fe occupation of the outer site. At zero temperature the value of $\langle c_{Fe}^{(out)} \rangle$ is determined by the lowest energy configuration in each case (compare with Fig. 3), i.e., zero Fe occupation of the outer site within PBEsol and within PBE using experimental lattice parameters, while $\langle c_{Fe}^{(out)} \rangle = 0.5$ for the fully relaxed PBE case, corresponding to all Fe cations sitting on an outer site. Furthermore, for $T \to \infty$ all three cases converge to a value of 0.25, which corresponds to a completely random distribution of Fe^{3+} cations over outer and inner sites. However, it can be seen that within the given approximations a fully random site occupancy is not reached even at temperatures significantly above 1000 K. Indeed, at a typical synthesis temperature of 1000 K (see, e.g., Refs. [21], [13], or [34]) less than 20% of outer sites are occupied by Fe^{3+} within PBEsol and when using experimental lattice parameters. This means that more than 60% of all Fe^{3+} cations can be found on the inner sites. Thus our results suggest that it is possible to alter the occupation of outer and inner sites by varying growth or sintering temperatures, cooling rates, and annealing times during synthesis.

Experimentally, while no indications for a deviation from the random distribution of Fe^{3+} and Ti^{4+} cations have been found in Rietveld refinements of neutron diffraction data [21], recent Mössbauer spectroscopy indicates a small preference of the Fe^{3+} cations for the inner perovskite sites [22], consistent with our PBEsol results. Lomanova *et al.* also found that this preferential occupation of inner (outer) sites with Fe^{3+} (Ti^{4+}) strengthens as the number of perovskitelike layers increases ($m \geqslant 5$) within the series $Bi_{n+1}Fe_{n-3}Ti_3O_{3n+3}$ [22], consistent with an earlier extended x-ray absorption fine structure (EXAFS) analysis of the five-layer system $Bi_6Fe_2Ti_3O_{18}$ [35]. A preferential occupation of the outer site with Ti^{4+} cations, has also been reported for the related system $Bi_5CrTi_3O_{15}$ [36].

It has been argued that the Ti^{4+} cation prefers the more distorted outer site because of its d^0 electron configuration, which exhibits a strong tendency for off-center displacement due to the second-order Jahn-Teller effect [37]. Interestingly, our relaxations show that, while it is, indeed, energetically more favorable that Fe occupies the inner site (at least within PBEsol and at the experimental volume), the presence of Fe^{3+} on the outer site in fact creates a significantly more distorted coordination octahedra compared to the Ti^{4+} cation (see the above discussion on local tetragonality). This strong local tetragonality, which resembles the local coordination found in $BiFeO_3$ films under strong compressive epitaxial strain [30,32,33], suggests that the Fe^{3+} cation also plays an active role in determining the site preference. The change in site preference with lattice constants seems to point towards competing tendencies between the individual site preferences of Fe^{3+} and Ti^{4+} cations.

Another possible explanation for the outer site preference of Ti^{4+}, suggested in Ref. [36], is that it is electrostatically more favorable to have the higher charged Ti^{4+} cation located closer to the negatively charged oxygen in the fluorite layer. Even though the importance of electrostatic effects cannot be strictly ruled out by our results, we point out that the pronounced dependence on lattice parameters and volume seems to indicate that changes in chemical bonding and coordination are more relevant than electrostatic effects.

Further insight in the underlying mechanism could be obtained by systematic studies of site preference as function of volume and strain, and by investigating different compositions where Fe^{3+} is replaced by other magnetic transition metal cations (see, for example, the case of $Bi_5CrTi_3O_{15}$ in Ref. [36]).

B. Internal structural parameters and mode decomposition

Next, we analyze the differences in the internal atomic coordinates of the various configurations listed in Table I. Due to the numerous internal degrees of freedom and different symmetries for the different configurations, we do not compare the individual atomic coordinates directly. Instead, we perform a symmetry mode decomposition of all relaxed structures, as well as of the experimentally observed structure, using the same high symmetry $I4/mmm$ reference structure in all cases (with equivalent atoms on all octahedrally coordinated sites). This allows for a more systematic quantitative comparison of the most relevant degrees of freedom [38].

The position of each atom $\vec{r}_i$ in the unit cell, can be written as the sum of its position in the high-symmetry reference structure $\vec{r}_i^{\,0}$ (here taken to be the paraelectric $I4/mmm$ structure) and a displacement vector $\vec{u}_i$:

$$\vec{r}_i = \vec{r}_i^{\,0} + \vec{u}_i. \tag{2}$$

The set of displacement vectors can then be expressed as linear combinations of *mode vectors* $\vec{\epsilon}_{i,m}$ with amplitudes A_m:

$$\vec{u}_i = \sum_m A_m \vec{\epsilon}_{i,m}. \tag{3}$$

Thereby, each mode vector can be chosen such that it transforms according to a single irreducible representation, characterized by the index m, of the symmetry group of the reference structure. In general, these mode vectors consist of several components—the symmetry-adapted modes basis for that irreducible representation, which correspond for example to displacements of cations on different Wyckoff positions. It is important not to confuse these displacement modes, which correspond to the distortion in the relaxed structure, with specific phonon eigenmodes.

In the following, we only discuss the *total* mode amplitude for each irreducible representation, which is calculated from the vectorial sum of all the individual components. For more details please refer to Ref. [38]. In the present work, the mode decomposition is performed using the tool AMPLIMODES available from the Bilbao Crystallographic Server [39].

There are three distinct symmetry modes that are involved in the transition from the paraelectric $I4/mmm$ group to the experimentally observed ferroelectric $A2_1am$ group: the polar Γ_5^- mode and two zone-boundary modes, X_3^- and X_2^+ (see Fig. 5). This is in direct analogy to the case of the two-layered Aurivillius system $SrBi_2Ta_2O_9$ [41], since the high- and low-symmetry groups of both cases are identical.

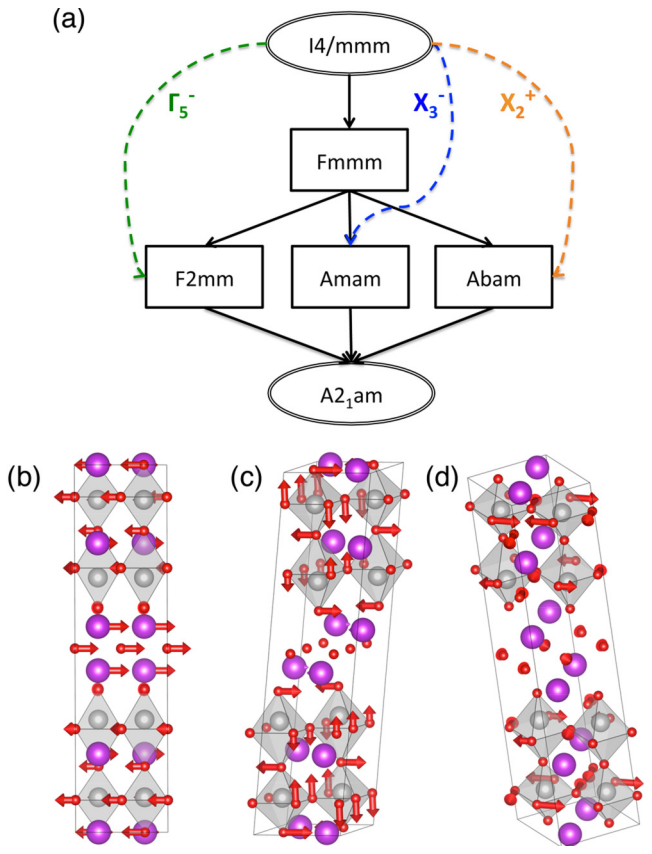

FIG. 5. (Color online) (a) Group-subgroup tree representing all possible ways of connecting the paraelectric $I4/mmm$ symmetry to the ferroelectric $A2_1am$ symmetry. Picture generated with the help of SUBGROUPGRAPH [40]. (b)–(d) Sketches of the three main distortion modes: Γ_5^-, X_3^-, and X_2^+, respectively. The displacement amplitudes of the various ions are indicated by the arrows. Different atoms are represented in the same way as in Fig. 1.

However, as stated in Sec. II A, the configurations we analyze in this work exhibit symmetries lower than $A2_1am$, and therefore contain additional distortion modes. Nevertheless, as already mentioned at the end of Sec. II A, we find that the departure from $A2_1am$ symmetry is small. In particular, we find that for all configurations the three modes listed above are the most dominant ones, in most cases with significantly larger amplitude than the "minor" modes related to the further symmetry lowering from $A2_1am$.

Figures 5(b)–5(d) shows the character of the three modes. These figures correspond to configuration M2, but the main features are similar for all configurations. It can be seen that the two zone-boundary modes, X_3^- and X_2^+, correspond to "tilts" of the oxygen octahedra within the perovskitelike layers around the in-plane [010] direction and "rotations" around the [001] direction, respectively. Furthermore, the polar Γ_5^- mode consists of an overall displacement of the ions in the Bi_2O_2 layer relative to the ions in the perovskite layer along the in-plane [010] direction. This resembles the so-called "rigid layer mode," which has been identified as the unstable polar mode in the two-layer Aurivillius system $SrBi_2Ta_2O_9$ [41,42]. Similar unstable (or very close to unstable) polar phonons have also been found in the one-layer system Bi_2WO_6 (Refs. [43,44]) and in the three-layer system $Bi_4Ti_3O_{12}$ [20,43]. Additional polar instabilities, corresponding to A-site or B-site displacive modes within the perovskite layer, have been identified for Bi_2WO_6 and $Bi_4Ti_4O_{12}$, respectively [20,43,44]. We note that the Γ_5^- mode depicted in Fig. 5 also exhibits a strong displacement of the B-site cations in the inner perovskite layer relative to the center of their coordination octahedra. An analysis of phonon instabilities in $Bi_5FeTi_3O_{15}$ would therefore be instructive to find further analogies or differences within the Aurivillius series. However, such an analysis is complicated to perform for $Bi_5FeTi_3O_{15}$, due to the lack of a well-defined high-symmetry configuration to be used in the calculations.

The amplitudes of the three main modes for all configurations are summarized in Fig. 6. It can be seen that even though there is some variation between the different configurations, the specific cation distribution does not have too strong an influence on the relative mode amplitudes. The most striking feature is the significant overestimation of the Γ_5^- mode amplitude within PBE. This effect can be related to the larger unit cell volume within PBE, and is thus very similar to the behavior found in many other ferroelectrics, where it has been shown that the ferroelectric mode is often very sensitive to the volume and generally becomes more dominant for larger volumes (see, e.g., Refs. [45–47]). On the other hand, there are only small differences between PBE and PBEsol for the two X modes. Taking into account both lattice parameters (Fig. 2) and mode amplitudes (Fig. 6), we can conclude that overall PBEsol leads to good agreement with the experimental structure reported in Ref. [21], and is therefore preferable to PBE for calculating the physical properties of $Bi_5FeTi_3O_{15}$ and related materials.

C. Electric polarization

We now calculate the spontaneous electric polarization of $Bi_5FeTi_3O_{15}$ using the so-called "Berry-phase" or "modern"

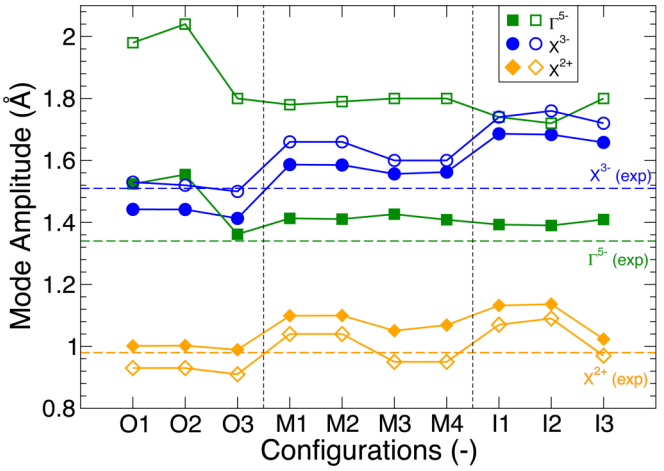

FIG. 6. (Color online) Amplitudes of the three main distortion modes in all considered configurations. Filled and open symbols correspond to PBEsol and PBE calculations, respectively. The dashed horizontal lines indicate experimental values from Ref. [21]. The full lines connecting points are simply guides to the eye.

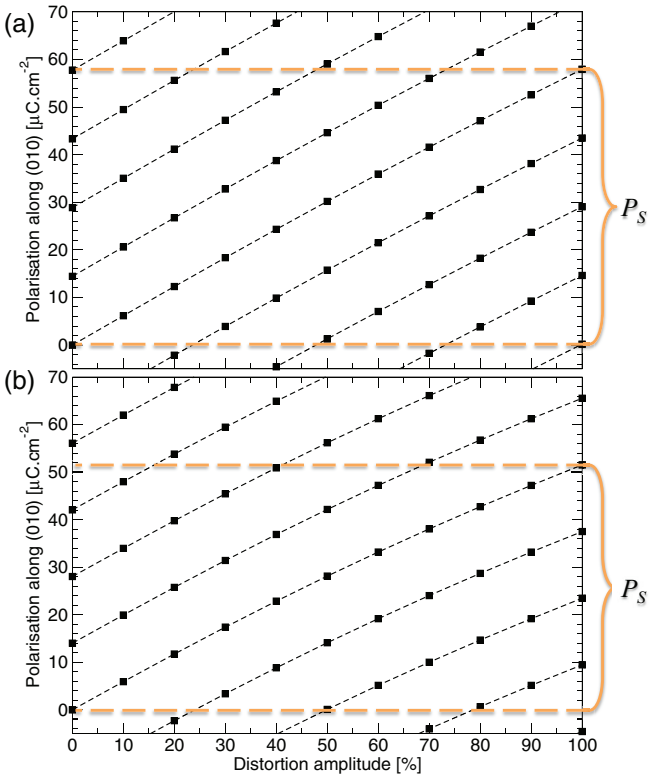

FIG. 7. (Color online) Change in polarization for increasing distortion from the centrosymmetric $P2_1/m$ structure to the relaxed ferroelectric structure with polar $P2_1$ symmetry calculated using PBEsol. Top (bottom) panel corresponds to configuration I1 (O1). All branches of the polarization lattice within a given range are shown. Points on the same branch are connected by lines. The magnitude of the spontaneous polarization P_s is also indicated (see main text).

theory of polarization [48–50]. According to this theory, the spontaneous polarization is defined as the difference in polarization between the ferroelectric ground state structure and a suitably defined centrosymmetric reference. In most cases, the paraelectric high-temperature phase provides a suitable reference structure for this purpose. However, in the case of $Bi_5FeTi_3O_{15}$ this corresponds to the tetragonal $I4/mmm$ structure shown in Fig. 1, which requires a random distribution of Fe and Ti cations over the different B sites within each perovskite layer. As discussed in Sec. II A the specific distributions of Fe and Ti considered in our calculations lead to symmetries lower than $I4/mmm$, in some cases even to polar symmetries. In the following, we therefore focus on two representative configurations, I1 and O1, corresponding to "inner" and "outer" cases, respectively. Both configurations correspond to distributions of Fe and Ti cations that do not break inversion symmetry and thus allow us to define suitable centrosymmetric reference structures.

These centrosymmetric reference structures are constructed by removing the polar Γ_5^-, the X_2^+, and all minor distortion modes from the fully relaxed ferroelectric structures. For both configurations, this leads to nonpolar $P2_1/m$ symmetry, whereas the corresponding fully relaxed structures have polar $P2_1$ symmetry. We note that the spontaneous polarization does not depend on a specific choice for the reference structure as long as the different reference structures can be transformed into each other by a continuous deformation that conserves the insulating character of the system and does not break inversion symmetry.

Another important consequence of the modern theory of polarization follows from the arbitrariness in the choice of the unit cell. As a result, the polarization inherits the periodicity of the crystal and is only determined modulo a *polarization quantum*, $\Delta P_Q = \frac{e\vec{R}}{\Omega}$, with e the electronic charge, Ω the volume of the unit cell, and $\vec{R}$ the shortest lattice vector along the polarization direction. Nevertheless, polarization differences between two structures that are related to each other by a small deformation are well defined as long as the corresponding change in polarization is small compared to the polarization quantum. If this is not the case, then intermediate deformations need to be considered until each polarization value can be unambiguously assigned to a specific "branch" of the "polarization lattice" (see, e.g., Ref. [51]). Note that in the present case the polarization quantum is rather small, $\Delta P_Q \sim 14\ \mu C/cm^2$, since the unit cell volume is quite large (due to the large unit cell length along $\vec{c}$), whereas the polarization is pointing along the short in-plane direction $\vec{b}$.

Figure 7 shows the calculated polarization using PBEsol for the two selected configurations as a function of the distortion amplitude connecting the centrosymmetric reference (0% distortion amplitude) with the fully relaxed ferroelectric structure (100% distortion amplitude). For each distortion amplitude we have included all values of the polarization lattice within a given range, the differences being exactly equal to the polarization quantum defined above. In order to identify the polarization values at different distortion amplitudes that correspond to the same branch of the polarization lattice (i.e., how to connect the individual points in Fig. 7 by lines), we evaluate a point charge estimate of the polarization using the formal charges of the ions (Bi^{3+}, Fe^{3+}, Ti^{4+}, O^{2-}). While this might give only a rough estimate of the magnitude of the spontaneous polarization, it clearly shows whether a

TABLE II. Spontaneous polarization P_s (calculated using the Berry phase approach) and point charge estimate P_{pc} (based on formal ionic charges) together with the amplitude of the polar Γ_5^- mode for the two representative configurations, O1 and I1, calculated using PBE and PBEsol energy functionals.

		P_s (μC/cm^2)	P_{pc} (μC/cm^2)	Γ_5^- (Å)
O1	PBE	60.3	39.1	1.97
	PBEsol	51.5	33.6	1.52
I1	PBE	66.3	43.9	1.73
	PBEsol	57.9	36.7	1.39

positive or negative change in polarization is expected with increasing distortion. In the present case, this is sufficient to make an unambiguous assignment of branches without the need to consider further intermediate distortion amplitudes. The resulting branches are indicated by lines in Fig. 7. The spontaneous polarization P_s corresponds to the difference between 0 and 100% distortion evaluated on the same branch. It can be seen that the polarization quantum (i.e., the distance between two neighboring branches) is indeed significantly smaller than P_s.

The obtained spontaneous polarizations, P_s, together with the point charge estimates, P_{pc}, and the Γ_5^- mode amplitudes for both configurations, calculated using both PBE and PBEsol, are listed in Table II. In all cases we obtain large values for P_s between 52 and 66 μC/cm^2. Due to the overestimation of the Γ_5^- mode amplitude within PBE compared to experiment (1.34 Å), we expect the spontaneous polarization calculated using the PBEsol functional to be more accurate. We thus predict a spontaneous polarization of $Bi_5FeTi_3O_{15}$ around 55 μC/cm^2.

While this is larger than what has been observed so far experimentally (see, e.g., Refs. [14] and [13]), it is quite similar to the spontaneous polarization for the closely-related three-layer Aurivillius compound $Bi_4Ti_3O_{12}$, as reported both from experiments ($P_S = 50$ μC/cm^2, Ref. [52]) and first-principles calculations ($P_S = 46$ μC/cm^2, Ref. [53]). The difference between our calculated $P_s \sim 55$ μC/cm^2, and available experimental data are therefore likely due to the difficulty in measuring fully saturated polarization loops in $Bi_5FeTi_3O_{15}$.

We also observe that the polarization of the I1 configuration is about 10% larger than that of the O1 configuration, for both PBE and PBEsol. On the other hand, the amplitude of the polar Γ_5^- mode is larger for the O1 configuration. This indicates that the Γ_5^- mode is slightly more polar in the I1 configuration than in the O1 case, i.e., the mode effective charge (see, e.g., Ref. [54]) of the Γ_5^- mode differs somewhat for the two configurations.

Overall, there is only a moderate influence of the specific Fe distribution on the ferroelectric properties. Most importantly, the presence of the magnetic cation is not detrimental to the ferroelectric polarization, which remains large compared to other nonmagnetic Aurivillius compounds.

Finally, we note that the large difference between the polarization calculated using the Berry phase approach and the point charge estimate based on formal charges indicates a highly anomalous value of the mode effective charge, which is enhanced by about 50%–60% compared to its formal value. Such enhanced effective charges are indicative of ferroelectricity that is driven by hybridization effects [54].

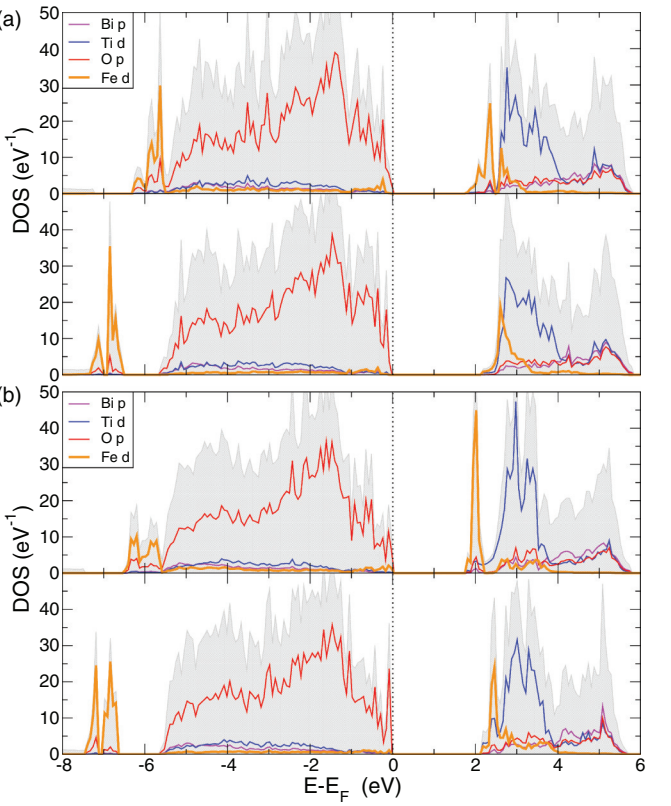

FIG. 8. (Color online) Total (gray shaded) and projected (lines) densities of states (DOS) for configurations O1 (a) and I1 (b) using different values of the Hubbard U parameter: $U_{Fe} = 3.0$ eV (top panel in each subfigure) and $U_{Fe} = 5.0$ eV (bottom panels).

D. Electronic structure

Figure 8 shows the electronic densities of states (DOS), total and projected on selected atomic and orbital characters, calculated using PBEsol for the two representative outer and inner configurations, O1 and I1. It can be seen that while there are some differences, the overall features of the densities of states are the same for the two cases. This indicates that the specific Fe/Ti distribution has only a marginal impact on the global electronic structure.

For both configurations, we obtain a large band gap of 1.7 eV (for $U_{Fe} = 3$ eV). The valence band is formed by states with predominant O-p character and the conduction band by states with predominant Ti/Fe-d character (and some Bi-p character at slightly higher energies). There is a strong splitting (~7.5 eV) between the Fe-d states with different local spin projection, consistent with a high spin d^5 electron configuration of Fe^{3+}. On the other hand, the Ti-d states are essentially empty (apart from small admixtures in the valence band due to hybridization with the O-p states), consistent with a d^0 configuration of the Ti^{4+} cation.

In order to test the impact of the Hubbard U parameter on the electronic structure, we compare the DOS obtained with $U_{Fe} = 3.0$ eV (the value used throughout this paper) with that obtained for a somewhat higher value of $U_{Fe} = 5.0$ eV. The larger U_{Fe} increases the spin splitting of the Fe-d states and pushes the unoccupied local minority spin Fe-d states to higher energies, so that the lower conduction band edge becomes more dominated by the Ti d states and the band gap increases to 2.1 eV. Note that an even larger value for U_{Fe} will not lead to a further increase of the band gap, which is then fixed by the energy difference between the occupied O p and unoccupied Ti d states.

Unfortunately, to the best of our knowledge, no spectroscopic data are available for $Bi_5FeTi_3O_{15}$ that would allow to identify the orbital character of the lower conduction band edge. Such data would be desirable to verify the correct description of the electronic structure of this material within the DFT+U approach and to narrow down the specific value for U_{Fe} to be used in such calculations.

E. Magnetic coupling constants

In this section, we calculate the strength and character of the magnetic coupling between the Fe cations in different relative positions. For this purpose, we fully relax all atomic positions and lattice parameters in each configuration for two different relative alignments of the magnetic moments of the two Fe^{3+} cations within the unit cell: (i) parallel, i.e., ferromagnetic (FM) alignment, and (ii) antiparallel, i.e., antiferromagnetic (AFM) alignment. Figure 9 shows the resulting total energies calculated using PBEsol (PBE leads to very similar results).

It can be seen that for all configurations where the two Fe^{3+} cations are in nearest-neighbor (NN) positions within the perovskite layer (O3, M4, I2, and I3), there is a large energy difference between the FM and the AFM case. For the two configurations where the Fe^{3+} cations are in next-nearest-neighbor (NNN) positions (M3 and I1), there is only a small energy difference between FM and AFM, whereas in all other configurations the energy differences are negligible. In all cases (even those with essentially negligible energy difference between FM and AFM), the AFM orientation has lower energy than the FM orientation.

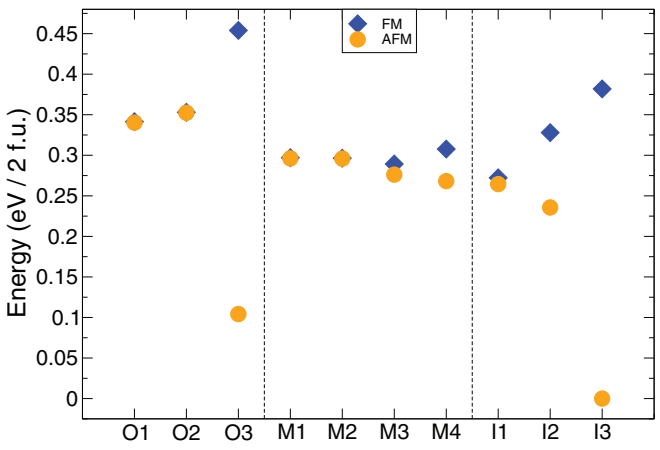

FIG. 9. (Color online) Energies of all configurations for FM (blue squares) and AFM (red circles) orientation of the Fe magnetic moments, within PBEsol.

TABLE III. Calculated magnetic Heisenberg coupling constants for nearest and next-nearest-neighbor coupling between the Fe^{3+} cations. Also listed are the corresponding (average) Fe-O bond distances, $d_{Fe\text{-}O}$, and the deviation, $\Delta\phi$, of the Fe-O-Fe bond angle from the ideal value of 180° for the nearest-neighbor configurations. Upper part (rows 2–4) corresponds to PBE calculations, lower part (rows 5–7) to PBEsol calculations.

configuration	I2	M4	I3	O3	I1	M3
J (meV)	43.0	11.8	42.3	39.7	0.9	1.5
$d_{Fe\text{-}O}$ (Å)	2.04	2.29	2.04	2.04	–	–
$\Delta\phi$ (°)	28.71	24.12	33.27	41.90	–	–
J (meV)	46.1	19.8	47.7	43.7	1.0	1.7
$d_{Fe\text{-}O}$ (Å)	2.03	2.20	2.00	1.99	–	–
$\Delta\phi$ (°)	27.48	22.45	32.74	41.53	–	–

The strong NN coupling and the rather short range of the magnetic coupling is indicative of the superexchange mechanism, which is generally the dominant magnetic coupling mechanism in insulating oxides such as $Bi_5FeTi_3O_{15}$. Furthermore, the preferred AFM alignment between NN cations is consistent with the Goodenough-Kanamori rules for the Fe^{3+} cation with a d^5 electron configuration [55,56].

For a more quantitative analysis of the strength of the magnetic coupling, we extract coupling constants J_{ij} by mapping the calculated energy differences onto a Heisenberg model, $E = \sum_{\langle ij \rangle} J_{ij} \hat{e}_i \hat{e}_j$, where the sum is over all "bonds" and the normalized vector $\hat{e}_i$ indicates the direction of the magnetic moment of the magnetic ion with index i. For this purpose, both FM and AFM energies are calculated using the relaxed structures obtained with AFM alignment of magnetic moments, in order to remove the structural component from the determination of the magnetic coupling constants. Since we consider only coupling between Fe in NN and NNN positions, each coupling constant is associated with exactly one particular ionic configuration. The resulting coupling constants are summarized in Table III.

We obtain rather strong nearest-neighbor couplings of the order of $J_{NN} \sim 40$–50 meV (except for configuration M4) and relatively weak next-nearest-neighbor coupling of $J_{NNN} \sim$ 1–2 meV. The couplings are slightly stronger in PBEsol compared to PBE, due to the slightly smaller bond distances within PBEsol. However, the differences between the two functionals are not very large. The nearest-neighbor coupling between inner and outer perovskite layers (configuration M4) is smaller than the other three nearest-neighbor couplings due to the strong sensitivity of the superexchange interaction to the bond distances and bond angles connecting the two coupled magnetic cations. The Fe-O bond distances, averaged over the two Fe-O bonds connecting two nearest-neighbor Fe cations ($d_{Fe\text{-}O}$), and the corresponding Fe-O-Fe bond angles ($\Delta\phi$) are also listed in Table III. It can be seen that the average Fe-O bond-length between adjacent inner and outer Fe sites is significantly larger for configuration M4 than for the other nearest-neighbor configurations. This is related to the strong elongation of the oxygen octahedra surrounding the outer Fe site.

The calculated nearest-neighbor coupling between the Fe cations in $Bi_5FeTi_3O_{15}$ is comparable in both sign and magnitude to the coupling in $BiFeO_3$, $J = 50.3$ meV, which we calculate using PBEsol and $U_{Fe} = 3$ eV (compare also to Ref. [57]). We also evaluate the impact of the Hubbard U parameter on the strength of the magnetic coupling by recalculating the coupling constants for $U_{Fe} = 5.0$ eV using PBE. This has the effect of reducing the average J by $\sim$30%. For example, the magnetic coupling corresponding to configuration I2 is $J = 43.0$ eV with $U_{Fe} = 3$ eV, and becomes $J = 31.2$ eV using $U_{Fe} = 5$ eV. Such a decrease of the magnetic coupling strength with U_{Fe} is expected with superexchange as the dominant coupling mechanism. Within the simplest model of superexchange, the coupling strength is proportional to t^2/U [55], where t is the effective hopping between Fe-d-like Wannier states and U is the corresponding Hubbard interaction parameter. While there is no direct correspondence between this U and U_{Fe} used in the DFT+U calculations, this simple picture is sufficient to explain the overall decrease of the magnetic coupling constants with U_{Fe}.

Due to the relatively low concentration of magnetic cations in $Bi_5FeTi_3O_{15}$ (25% on the octahedrally coordinated perovskitelike sites) and the short range of the magnetic superexchange interaction, it is unclear whether magnetic long range order can occur in this system. One requirement for long-range order is that percolation can be achieved throughout the material, i.e., the majority of Fe cations need to be connected with each other through continuous links between coupled neighbors. In a three-dimensional simple cubic lattice, to which the four-perovskite thick layers can be related, the threshold for percolation is 31% of magnetic sites when considering only NN couplings, and 14% with both NN and NNN couplings [58]. Thus, with 25% of magnetic sites as in $Bi_5FeTi_3O_{15}$, percolation is dependent on the rather weak NNN coupling, which will probably give rise to magnetic order only at rather low temperatures. Furthermore, the perovskitelike layers are separated by Bi_2O_2 layers that do not contain any magnetically active ions. The shortest superexchange path connecting two Fe cations on opposite sides of the Bi_2O_2 layer is of the form Fe-O-O-O-Fe, containing two O-O links, which will only give rise to a very weak coupling.

We can obtain a first estimate of the strength of this coupling from the energy difference between FM and AFM orientations for configuration O1. This energy difference is directly related to the interlayer coupling if one assumes that the coupling of the two Fe^{3+} cations through the perovskite layer is negligible. This seems reasonable, since the corresponding superexchange path involves a total of eight transition metal-oxygen bonds. We obtain $J_{interlayer} = 0.3$ meV, which is small but comparable with the weak next-nearest-neighbor coupling. However, we note that further calculations with a doubled unit cell containing 96 atoms are necessary to double check this result and obtain a more accurate estimate of the interlayer coupling.

IV. SUMMARY AND CONCLUSIONS

In summary, we have calculated from first-principles the basic stuctural, ferroelectric, and magnetic properties of the Aurivillius phase $Bi_5FeTi_3O_{15}$. We have also addressed a potential site preference of the Fe^{3+} and Ti^{4+} cations within the perovskitelike layers and discussed the possibility for magnetic long-range order within this material.

After systematically comparing our results obtained within PBE and PBEsol with available experimental data, we conclude that the PBEsol exchange-correlation functional provides an excellent description of the structural degrees of freedom in $Bi_5FeTi_3O_{15}$, superior to PBE, and we suggest to use PBEsol for further DFT studies of related members of the Aurivillius family.

Our results show that there is a preference for the Fe^{3+} cations to occupy the inner sites within the perovskitelike layers, consistent with recent Mössbauer data [22]. We have also shown that this site preference depends strongly on the lattice constants and reverses to an outer site preference for the slightly more extended lattice parameters within PBE. In addition, the c/a ratio of the crystallographic unit cell is systematically larger for configurations where Fe^{3+} occupies the outer sites. This suggests the possibility to control the site occupancies via epitaxial strain in thin films of $Bi_5FeTi_3O_{15}$.

Moreover, we calculate a large value of 55 $\mu C/cm^2$ for the spontaneous electric polarization, which shows that the presence of the nominally nonferroelectric magnetic Fe^{3+} cation does not impede the ferroelectricity in this Aurivillius system.

Finally, we show that there is a strong antiferromagnetic coupling between Fe^{3+} cations in nearest-neighbor positions, characteristic of the superexchange interaction between d^5 cations, but that the coupling between further neighbors is rather weak and essentially becomes negligible beyond second neighbors. With a concentration of 25% magnetic cations on the perovskite B site, the system is above the percolation threshold for a simple cubic lattice with both NN and NNN interactions, but it is unclear how the interlayer Bi_2O_2 layers will influence percolation in the Aurivillius structure and what ordering temperature can be expected based on the weak NNN coupling. In addition, it is likely that the percolation within the perovskite layers depends critically on the distribution of magnetic cations within these layers. The possibility to control this distribution either by strain or by changing preparation conditions, as discussed in Sec. III A, could therefore be crucial for achieving magnetic long range order in $Bi_5FeTi_3O_{15}$ and related Aurivillus systems.

We note that even with a relatively weak interlayer coupling, long range order at elevated temperatures can in principle be achieved if the magnetic moments within the perovskite layers are highly correlated (due to strong magnetic coupling *within* these layers). In this case, all weak interlayer couplings will add up constructively and lead to a relatively strong effective coupling between the layers. Such behavior has been studied for example in the context of the anisotropic quasi-two-dimensional Heisenberg model (see, e.g., Ref. [59]).

It therefore seems that, in order to achieve robust magnetic order above room temperature, a higher concentration of magnetic ions would be desirable, which would lead to stronger coupling within the perovskite layers. One obstacle for achieving such higher concentrations of magnetic cations is the relation between the average valence of the B-site

cations and the number of perovskite layers m throughout the Aurivillius series. With a formal charge of 3+ on the A site (corresponding to Bi^{3+}) the required average valence on the B site varies from 4+ for $m = 3$ to 3+ for $m \to \infty$. The possibility to substitute Mn^{4+} for Ti^{4+} in the three-layer structure has been studied computationally by Tinte and Stachiotti [60]. However, they found only incipient ferroelectricity in the fully substituted system $Bi_4Mn_3O_{12}$. Furthermore, the Mn^{4+} cation has a rather small ionic radius, which falls outside the range that is considered suitable for incorporation on the B site of the Aurivillius structure [7]. Magnetic cations that are suitable for incorporation on the B site within the Aurivillius structure generally have charge states of only 3+ or even 2+. One possible route to increase the concentration of magnetic cations is therefore to focus on compositions with a higher number of perovskite layers, i.e., $m > 4$. Indeed, magnetic long range order has been reported for several $m = 5$ systems [12,18]. Another possibility to increasing the Fe^{3+} content (or more generally the content of magnetic 3+ cations) in the $m = 4$ layer system would be to simultaneously replace Ti^{4+} by other B-site cations with higher valence, such as Ta^{5+}, Nb^{5+}, or W^{6+}, leading to compositions such as $Bi_5Fe_{1+x}Ti_{3-2x}Nb_xO_{15}$.

We conclude, that the Aurivillius family is a promising class of compounds to search for new multiferroics with good ferroelectric and magnetic properties. The main challenge is to increase the content of magnetic cations, in order to obtain robust magnetic long range order at elevated temperatures. The Aurivillius family provides enough chemical flexibility to explore new compositions that are promising in that respect. Our results indicate that it is conceivable to have ferroelectricity coexist with long-range magnetic order, and we hope that our work will stimulate further research on Aurivillius compounds as potential room-temperature multiferroics.

ACKNOWLEDGMENTS

This work was supported by the Swiss National Science Foundation under project no. 200021_141357, by ETH Zürich, and by Science Foundation Ireland through the FORME project. We thank Lynette Keeney, Roger Whatmore, and Martyn Pemble from the Tyndall National Institute in Cork, Ireland, for many important discussions and for pointing our attention to the Aurivillius phases as potential multiferroics. We also thank Eric Bousquet for many useful discussions.

[1] N. A. Spaldin and M. Fiebig, Science **309**, 391 (2005).
[2] W. Eerenstein, N. D. Mathur, and J. F. Scott, Nature (London) **442**, 759 (2006).
[3] S.-W. Cheong and M. Mostovoy, Nat. Mater. **6**, 13 (2007).
[4] R. Ramesh and N. A. Spaldin, Nat. Mater. **6**, 21 (2007).
[5] N. A. Spaldin, S.-W. Cheong, and R. Ramesh, Phys. Today **63**, 38 (2010).
[6] K. Momma and F. Izumi, J. Appl. Crystallogr. **44**, 1272 (2011).
[7] R. E. Newnham, R. W. Wolfe, and J. F. Dorrian, Mat. Res. Bull. **6**, 1029 (1971).
[8] C. A. Paz de Araujo, J. D. Cuchiaro, L. D. McMillan, M. C. Scott, and J. F. Scott, Nature (London) **374**, 627 (1995).
[9] B. H. Park, B. S. Kang, S. D. Bu, T. W. Noh, J. Lee, and W. Jo, Nature (London) **401**, 682 (1999).
[10] X. Mao, W. Wang, X. Chen, and Y. Lu, Appl. Phys. Lett. **95**, 082901 (2009).
[11] X. Chen, J. Xiao, Y. Xue, X. Zeng, F. Yang, and P. Su, Ceram. Int. **40**, 2635 (2014).
[12] L. Keeney, T. Maity, M. Schmidt, A. Amann, N. Deepak, N. Petkov, S. Roy, M. E. Pemble, and R. W. Whatmore, J. Am. Ceram. Soc. **96**, 2339 (2013).
[13] W. Bai, J. Zhu, J. Wang, T. Lin, J. Yang, X. Meng, X. Tang, Z. Zhu, and J. Chu, J. Magn. Magn. Mater. **324**, 2265 (2012).
[14] X. Mao, W. Wang, H. Sun, Y. Lu, and X. Chen, J. Mater. Sci. **47**, 2960 (2012).
[15] L. Keeney, S. Kulkarni, N. Deepak, M. Schmidt, N. Petkov, P. F. Zhang, S. Cavill, S. Roy, M. E. Pemble, and R. W. Whatmore, J. Appl. Phys. **112**, 052010 (2012).
[16] A. Srinivas, S. V. Suryanarayana, G. S. Kumar, and M. M. Kumar, J. Phys.: Condens. Matter **11**, 3335 (2011).
[17] X. W. Dong, K. F. Wang, J. G. Wan, J. S. Zhu, and J.-M. Liu, J. Appl. Phys. **103**, 094101 (2008).
[18] E. Jartych, T. Pikula, M. Mazurek, A. Lisinska-Czekaj, D. Czekaj, K. Gaska, J. Przewoznik, C. Kapusta, and Z. Surowiec, J. Magn. Magn. Mater. **342**, 27 (2013).
[19] G. Chen, W. Bai, L. Sun, J. Wu, Q. Ren, W. Xu, J. Yang, X. Meng, X. Tang, C.-G. Duan *et al.*, J. Appl. Phys. **113**, 034901 (2013).
[20] J. M. Perez-Mato, P. Blaha, K. Schwarz, M. Aroyo, D. Orobengoa, I. Etxebarria, and A. Garcia, Phys. Rev. B **77**, 184104 (2008).
[21] C. H. Hervoches, A. Snedden, R. Riggs, S. H. Kilcoyne, P. Manuel, and P. Lightfoot, J. Solid State Chem. **164**, 280 (2002).
[22] N. Lomanova, V. Semenov, V. Panchuk, and V. Gusarov, J. Alloys Comp. **528**, 103 (2012).
[23] G. Kresse and J. Furthmüller, Comput. Mater. Sci. **6**, 15 (1996).
[24] G. Kresse and D. Joubert, Phys. Rev. B **59**, 1758 (1999).
[25] J. P. Perdew, K. Burke, and M. Ernzerhof, Phys. Rev. Lett. **77**, 3865 (1996).
[26] J. P. Perdew, A. Ruzsinszky, G. I. Csonka, O. A. Vydrov, G. E. Scuseria, L. A. Constantin, X. Zhou, and K. Burke, Phys. Rev. Lett. **100**, 136406 (2008).
[27] V. I. Anisimov, F. Aryasetiawan, and A. I. Liechtenstein, J. Phys.: Condens. Matter **9**, 767 (1997).
[28] J. B. Neaton, C. Ederer, U. V. Waghmare, N. A. Spaldin, and K. M. Rabe, Phys. Rev. B **71**, 014113 (2005).
[29] I. A. Kornev, S. Lisenkov, R. Haumont, B. Dkhil, and L. Bellaiche, Phys. Rev. Lett. **99**, 227602 (2007).
[30] A. J. Hatt, N. A. Spaldin, and C. Ederer, Phys. Rev. B **81**, 054109 (2010).
[31] O. Diéguez, O. E. González-Vázquez, J. C. Wojdeł, and J. Íñiguez, Phys. Rev. B **83**, 094105 (2011).
[32] R. J. Zeches, M. D. Rossell, J. X. Zhang, A. J. Hatt, Q. He, C.-H. Yang, A. Kumar, C. H. Wang, A. Melville, C. Adamo, G. Sheng, Y.-H. Chu, J. F. Ihlefeld, R. Erni, C. Ederer, V. Gopalan, L. Q. Chen, D. G. Schlom, N. A. Spaldin, L. W. Martin, and R. Ramesh, Science **326**, 977 (2009).
[33] H. Béa, B. Dupé, S. Fusil, R. Mattana, E. Jacquet, B. Warot-Fonrose, F. Wilhelm, A. Rogalev, S. Petit, V. Cros, A. Anane,

F. Petroff, K. Bouzehouane, G. Geneste, B. Dkhil, S. Lisenkov, I. Ponomareva, L. Bellaiche, M. Bibes, and A. Barthélémy, Phys. Rev. Lett. **102**, 217603 (2009).
[34] S. Nakashima, H. Fujisawa, S. Ichikawa, J. M. Park, T. Kanashima, M. Okuyama, and M. Shimizu, J. Appl. Phys. **108**, 074106 (2010).
[35] M. E. Montero-Cabrera, M. Garcia-Guaderrama, A. Mehta, S. Webb, L. Fuentes-Montero, J. A. Duarte Moller, and L. Fuentes-Cobas, Rev. Mex. Fís. S **54**, 42 (2008).
[36] A. T. Giddings, M. C. Stennett, D. P. Reid, E. E. McCabe, C. Greaves, and N. C. Hyatt, J. Solid State Chem. **184**, 252 (2011).
[37] I. B. Bersuker, *Electronic Structure and Properties of Transition Metal Compounds* (Wiley, Hoboken, 2010).
[38] J. M. Perez-Mato, D. Orobengoa, and M. I. Aroyo, Acta Cryst. A **66**, 558 (2010).
[39] D. Orobengoa, C. Capillas, M. I. Aroyo, and J. M. Perez-Mato, J Appl. Cryst. **42**, 820 (2009).
[40] S. Ivantchev, E. Kroumova, G. Madariaga, J. M. Perez-Mato, and M. Aroyo, J. Appl. Crystallogr. **33**, 1190 (2000).
[41] J. M. Perez-Mato, M. Aroyo, A. García, P. Blaha, K. Schwarz, J. Schweifer, and K. Parlinski, Phys. Rev. B **70**, 214111 (2004).
[42] M. G. Stachiotti, C. O. Rodriguez, C. Ambrosch-Draxl, and N. E. Christensen, Phys. Rev. B **61**, 14434 (2000).
[43] R. Machado, M. G. Stachiotti, R. L. Migoni, and A. H. Tera, Phys. Rev. B **70**, 214112 (2004).
[44] H. Djani, E. Bousquet, A. Kellou, and P. Ghosez, Phys. Rev. B **86**, 054107 (2012).
[45] P. Ghosez, X. Gonze, and J.-P. Michenaud, Europhys. Lett. **33**, 713 (1996).
[46] S. Bhattacharjee, E. Bousquet, and P. Ghosez, Phys. Rev. Lett. **102**, 117602 (2009).
[47] C. Ederer, T. Harris, and R. Kováčik, Phys. Rev. B **83**, 054110 (2011).
[48] R. D. King-Smith and D. Vanderbilt, Phys. Rev. B **47**, 1651 (1993).
[49] D. Vanderbilt and R. D. King-Smith, Phys. Rev. B **48**, 4442 (1993).
[50] R. Resta, Rev. Mod. Phys. **66**, 899 (1994).
[51] N. A. Spaldin, J. Solid State Chem. **195**, 2 (2012).
[52] S. E. Cummins, J. Appl. Phys. **39**, 2268 (1968).
[53] S. H. Shah and P. D. Bristowe, J. Phys.: Condens. Matter **22**, 385902 (2010).
[54] P. Ghosez, J. P. Michenaud, and X. Gonze, Phys. Rev. B **58**, 6224 (1998).
[55] P. W. Anderson, in *Magnetism*, edited by G. T. Rado and H. Suhl (Academic Press, New York, 1963), Vol. 1, Chap. 2, pp. 25–83.
[56] J. B. Goodenough, *Magnetism and the Chemical Bond* (Interscience, New York, 1963).
[57] P. Baettig, C. Ederer, and N. A. Spaldin, Phys. Rev. B **72**, 214105 (2005).
[58] L. Kurzawski and K. Malarz, Rep. Math. Phys. **70**, 163 (2012).
[59] C. Yasuda, S. Todo, K. Hukushima, F. Alet, M. Keller, M. Troyer, and H. Takayama, Phys. Rev. Lett. **94**, 217201 (2005).
[60] S. Tinte and M. G. Stachiotti, Phys. Rev. B **85**, 224112 (2012).